Flexural-tensegrity snapping tails for bio-inspired propulsion in fluids

Claudio Boni [a], Pedro M. Reis [b], Gianni Royer-Carfagni [a,c,*]

[a] *Department of Engineering and Architecture, University of Parma, Parco Area delle Scienze 181/A, I-43100 Parma, Italy*
[b] *Flexible Structures Laboratory (fleXLab), École Polytechnique Fédérale de Lausanne (EPFL), Rte Cantonale, CH-1015 Lausanne, Switzerland*
[c] *Construction Technologies Institute - Italian National Research Council (ITC-CNR), Via Lombardia 49, I-20098 San Giuliano Milanese, Milano, Italy*

ARTICLE INFO

ABSTRACT

Many aquatic animals propel themselves by flapping their tails. Leveraging a recently proposed snapping cantilever beam based on the concept of flexural tensegrity, we propose a bio-inspired propulsion device. The design comprises a segmental beam with hollow voussoirs in unilateral contact along tailor-shaped surfaces, held together by a prestressed internal cable. Prescribing relative periodic rotation to a pair of consecutive control segments of the structured beam produces multi-articulated sequential snapping of all joints. We built a series of prototypes and performed precision experimental tests in water to characterize their propulsive capacity. A parametric study was carried out to characterize the dependence of the thrust produced by the oscillating tail on the following factors: number of segments, shape of the internal cavities dictating the cantilever curvature, and mobility constraint of a fin appended at the end of the tail. The results provide a proof of concept that our design for a snapping structured beam can be used as a propulsive device. We further demonstrate the feasibility of this propulsion unit to propel a toy boat in a water basin.

© 2022 Elsevier Ltd. All rights reserved.

1. Introduction

Cephalopods, fish, and aquatic mammals are extraordinary examples of how nature can find efficient strategies for propulsion in a fluid environment [1–3]. Focusing on fish, two main modes of swimming can be identified, generally related to the shape of their body [4]. In slender-bodied fishes, such as eels, the whole lissome body tends to undulate at high amplitude in the so-called *anguilliform* mode. By contrast, fishes with a broad tail, compact body, and narrow caudal peduncle generally swim in the *carangiform* mode, oscillating only their tail [5]. These different swimming modes produce distinct vortex and wake structures in the fluid, with varying efficiencies. Experimental and computational results [4] show that carangiform swimmers are more efficient at high swimming speeds, while the anguilliform mode is preferable at low speeds.

Nature has long been a source of inspiration for artificial swimming devices. The robotic tuna [6] is a pioneering example of an efficient swimming machine but, even if the body shape and the swimming mode closely mimicked real tuna fish, the actuation was done with motors outside the testing tank. Recent advances in bio-inspired soft robotics and miniaturization [7] have enabled fish-like semi-autonomous robots for underwater

exploration [8,9]. Flexible oscillating tails for propulsion proved to be feasible also for *silent* operations of larger vessels [10]: moving fins minimize cavitation noise, which instead characterizes standard helix-based propellers. Indeed, the search for noise reduction or, more precisely, for low-level noise resembling a *biological sound*, is one of the goals of naval designers for stealth vessels and robotic rovers used for the exploration of natural environments. This context has motivated us to investigate the propulsion capacity of an oscillating tail in water.

Our design adopts a recently proposed mechanism [11] within the class of flexural-tensegrity structures. The term "*flexural tensegrity*" [12] was coined to indicate beam-like structures formed by rigid segments held together by an elastic prestressed cable, whose tying action provides the *integrity under flexure* to the assembly. The key aspect in this structural system is that the contact surfaces between any two consecutive segments are curved and shaped according to properly designed pitch lines. As such, each joint opens up due to the relative rotation of the segments. This classification is not to be confused with post-tensioned segmental beams used in precast concrete bridges [13], for which the contact surfaces are approximately planar, and no opening of the joints is expected in the serviceability limit state. The cable, hosted and constrained to move in properly shaped cavities inside the segments, is anchored only to the end segments and is free to slide inside the beam. Opening the joints causes stretching of the cable to an extent dictated by the shape of contact surfaces, thereby modifying the elastic energy

stored in the system and, in turn, setting its constitutive bending properties.

The concept of flexural-tensegrity beams has been explored in many forms. By changing the shape of contact profiles, linear, sub-linear, or super-linear constitutive responses can be obtained [12]. Nonlinear Duffing-like vibrations can be realized and controlled [14], acting on tendon stiffness and prestress. If the mobility of the tendon inside the segments is modified, passing from a tubular sheath to a larger cavity, the bending energy can be made non-convex [15], enabling complex snap-through motions in response to localized perturbations [11]. The limit when the number of segments goes to infinity, and their length to zero, corresponds to a particular type of Euler's elastica [16] with nonlocal response. Field applications of flexural tensegrities, yet to be fully exploited, have been found in archery (*e.g.*, an innovative bow [17]) and soft robotics (*e.g.*, cable-controlled limbs with capabilities as in [18]). Multi-stable flexural tensegrities could also be used in robots for in-pipe traveling [19,20], or as basic constituents for metamaterials with tailored 3D mechanisms [21].

Here, we explore the applicability of the flexural-tensegrity concept [11] to make active flapping devices for propulsion in fluid media, focusing on carangiform-mode oscillating tails. To characterize the fluid–structure interaction, we perform precision experiments and measure the thrust generated by the oscillating tail in a water tank for different designs of the structure and the terminal fin, as the actuation frequency is varied. The device is simple and robust; the snapping is reversible and activated by a single cable; the actuation is a simple crank and crankshaft mechanism operated by a motor at low revs. A toy boat has been manufactured to demonstrate feasibility in the field. We believe that our innovative propulsion device, which differs from other active/passive non-snapping flappers, can find applications for swimming robots or silent vessels.

2. Definition of the problem

In Fig. 1(a), we present a schematic diagram of the mid-surface layout of our segmented beam, which adopts the design concept from [11]. A tapered cantilever of n hollow segments ($n = 7$ in Fig. 1) is held together by a pre-tensioned cable. The beam is clamped at the (fixed) segment $i = 2$, while the (control) segment $i = 1$ is rotated externally to trigger the snapping. The internal cavities, symmetric to the segment axis, are trapezoidal for the segments $2 \leq i \leq n - 1$, and triangular at $i = 1$ and $i = n$, with the anchoring point of the cable at the vertices (points S and H, in Fig. 1(a)). The contact surfaces are shaped according to circular pitch lines, with an equal radius for all joints; the toothed profiles prevent sliding. The cable is free to move inside the segments, constrained only by the cavity walls. This geometry makes the cable elongate by $\Lambda_i = \Lambda_i(\Delta\varphi_i)$ when segments i and $i + 1$ are relatively rotated by $\Delta\varphi_i$. As a result of the rotation of all joints, the total elongation of the cable is $\Lambda = \sum_{i=1}^{n-1} \Lambda_i$. Assuming that the segments are rigid, the variation of the elastic energy, due to the cable strain alone, reads

$$\Delta U = N_0 \left(\sum_{i=1}^{n-1} \Lambda_i(\Delta\varphi_i) \right) + \frac{1}{2}K \left(\sum_{i=1}^{n-1} \Lambda_i(\Delta\varphi_i) \right)^2 , \tag{1}$$

where N_0 represents the initial prestressing force and K is the effective axial stiffness of the cable.

The system is actuated by gradually rotating the segment $i = 1$, while segment $i = 2$ is kept fixed, causing the cable to move inside the cavities and elongate by Λ. Static equilibrium is attained as long as the cable passes through the pitch point of each joint $i \neq 1$ (condition of null lever arm), while Λ progressively increases (also increasing ΔU) until the equilibrium becomes unstable. At this point, Λ can be lowered by an
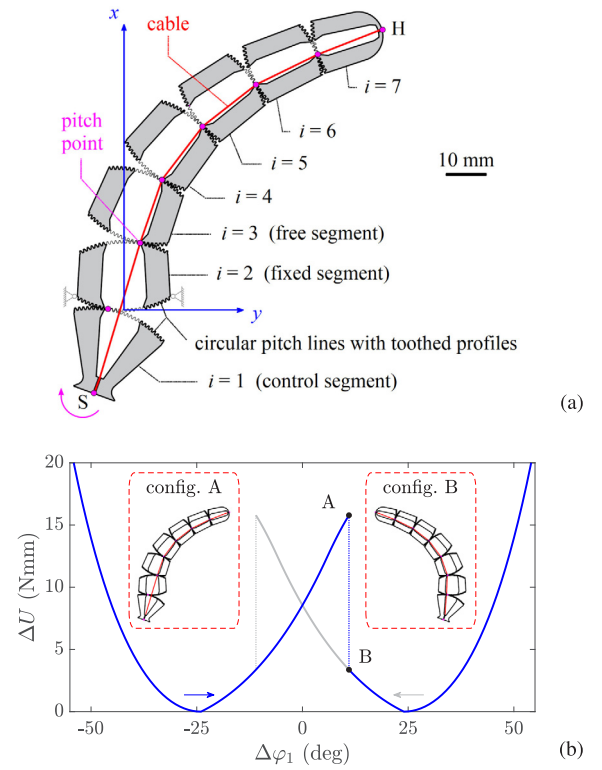
Fig. 1. Schematic of the tail structure and its energy paths. (a) Mid-surface layout of the structured beam comprising a series of 7 segments held together by a cable (red line), which can move within the internal cavity (central non-shaded regions) and is blocked by lateral walls (shaded regions) of each element. (b) Quasi-static energy landscape: when moving along the path of increasing $\Delta\varphi_1$ (in blue), snapping occurs between the complementary equilibrium configurations A and B. A video of the tail snapping in the air is provided as supplementary material; in this case, the tail is made of transparent acrylic, in order to appreciate the movement of the cable, made of black polypropylene, inside the segmental cavities. (For interpretation of the references to color in this figure legend, the reader is referred to the web version of this article.)

infinitesimal perturbation, and the structure snaps, reversing its shape from configuration A to B, represented in Fig. 1(b) together with the corresponding energy path. An orderly sequential snap of the contact joints ensues, because the relative rotation of a pair of consecutive segments produces the snapping of the adjacent joint. Cyclically changing the sign of rotation of the control segment drives the beam to reverse its shape, alternately, acting as an oscillating tail. We will interpret this oscillatory snapping motion for locomotion applications in fluid environments.

Fluid–structure interaction is a challenging problem to tackle predictively because of the non-trivial coupling of elastic, inertial, and fluid forces, which depend on time, geometry, and the physical properties of both fluid and structure. Developing analytical or computational models for this class of problem is particularly challenging in unsteady and turbulent flows, with added complexity in our system arising from the snap-though instability of the structure. Models for active/passive flexible/rigid flappers have been reported in the literature [22], but these usually consider simple geometries for the flapping foil, sinusoidal heave and pitch motions, small deflection theory, linearized terms, and inviscid fluid. Our system does not share the simple geometry of a rectangular plate, and it undergoes very large oscillations regulated by nonlinear contributions associated with the snap-through instability in a turbulent and dissipative medium. Therefore, the present study focuses exclusively on precision experiments aimed at a first quantitative characterization of the propulsive capacity.
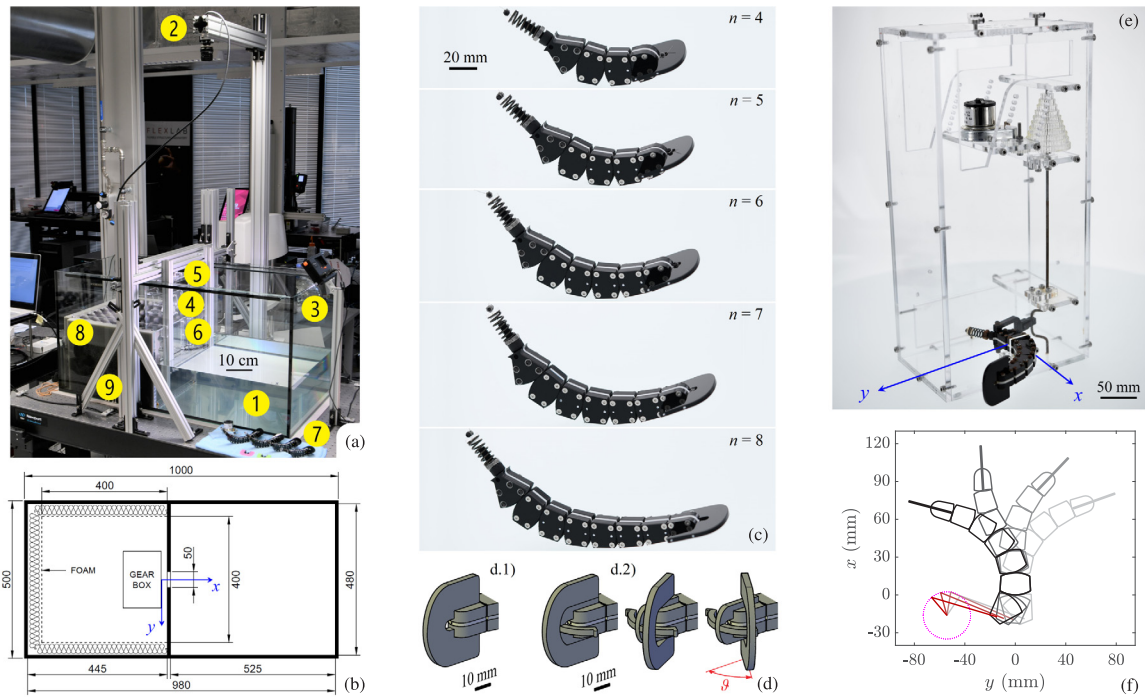
Fig. 2. Experimental setup and prototypes. (a) View of the setup with indication of: (1) the tank, (2) the camera, (3) the light, (4) the driving system, (5) the load sensor, (6) the separating barrier, (7) the prototypes to be tested, (8) the foam coating, and (9) the rigid lab frame. (b) Schematic plan view of the tank, with indication of the main dimensions [mm] and reference frame. (c) Tested prototypes with variable number n of segments. (d) Axonometric representation of the terminal fin: (d.1) fixed fin, clamped to the terminal segment; (d.2) pinned fin, in three different rotated configurations, with indication of the limit angle ϑ. (e) Detail of the driving system, mounted onto the load cell: the motor is connected through gears to a crankshaft and the snapping beam is actuated by a crank. (f) Schematic representation of the motion (actuating crank drawn in red color), reconstructed from the video recording of the experiments in water (a video of a demonstrative cantilever snapping in air is provided as supplementary material). (For interpretation of the references to color in this figure legend, the reader is referred to the web version of this article.)

3. Experimental apparatus

The photograph in Fig. 2(a) shows the experimental apparatus, which includes a $100 \times 50 \times 50$ cm^3 water tank (see Fig. 2(b) for additional dimensions) where the samples, connected to a driving system, were immersed. The driving system was mounted on the lab frame through a load cell to measure the reaction forces F_x and F_y (in the x and y directions reported in Figs. 1(a) and 2(b)) arising from the fluid–structure interaction.

The samples (prototypes) consist of n segments of length 17.8 mm with a pitch line radius of 24.0 mm. Each segment is composed of three laser-cut layers bolted together. The two external layers (see Fig. 2(c)) are made of *black* 6 mm-thick PMMA, shaped for the toothed contact profiles (indicated in Fig. 1(a)); the central *white* 2 mm-thick PMMA layer is cut to form the internal cavities. The cable is a Nitinol wire of diameter 20 μm. A steel compression spring (elastic constant 5.9 N/mm) is added in series to the wire at the anchoring point to increase its compliance and measure the initial prestress N_0 from the spring shortening. The beam stiffness can be tuned by increasing the prestress: the value of $N_0 = 9.0 \pm 1.2$ N was found to be an appropriate compromise between beam stiffness, matched with viscous and inertial forces that come into play, and strength of the various components.

Each of prototypes shown in Fig. 2(c) was equipped with a fin (see Fig. 2(d)) to the end segment $i = n$, perpendicularly to the mid-surface. This fin was made out of PMMA (thickness 3 mm) and was effectively rigid in the considered regime of fluid loading. The trailing edge was designed convex to enhance thrust generation [23]. The connection of the fin to the end segment, $i = n$, was either clamped (Fig. 2(d).1) or pinned (Fig. 2(d).2). The pinned fins are equipped with a stop, limiting the maximum rotation angle to ϑ.

As shown in Fig. 2(e), the segment $i = 2$ of the tail was bolted to a transparent PMMA box, the upper face of which was in turn connect to a load sensor (Schunk Mini40 SI-20-1), mounted on the test frame. This box housed the driving system comprising a gearbox coupled to both an electric 60 rpm 12 V DC motor (Cramer 30827) and a crankshaft, supporting the crank that cyclically rotated the segment $i = 1$ of the prototype. In Fig. 2(f), we present a schematic of the snapping of the tail, actuated by the crank. Multiple gears allowed us to vary the gear ratio with the motor, which ran at a constant velocity, in order to change the actuation frequency.

The tank was filled with water at room temperature (≈ 20 °C) up to a height of 18 cm, so that the tail was fully submerged, 5 cm below the free surface. The tank was divided into two basins (see Fig. 2(b)). The actuating system was hosted in the left-hand partition, whose lateral walls were coated with foam panels to minimize contamination of the force signals due to wave reflections. The tail was placed on the right-hand partition. The separating barrier between the left- and right-hand partitions contained an aperture where the tail passed through. In the absence of a background flow, the Reynolds number was estimated [24,25] as Re $= 2\pi f A L / \nu$, where L is the length of the oscillating tail from the clamped segment, A is the tip amplitude, f is the actuation frequency and $\nu = 1 \cdot 10^{-6}$ m^2/s is the kinematic viscosity of water. For our typical experimental values ($A \simeq 60$ mm, $L \simeq 90$ mm, and $f \simeq 1$ Hz) one finds Re $\simeq 34\,000$.

During the experiments, we measured the reaction forces F_x and F_y (x and y directions as per Fig. 1(a)) experienced by the driving box, connected to an external rigid frame (Fig. 2(a)) through the load sensor. Given that the tail is integral with the box at segment $i = 2$, these forces are equivalent to the longitudinal

(thrust) and transverse forces generated by the prototype oscillating in water. In particular, we performed a parametric study to investigate how the thrust is influenced by the number of segments n, the type of terminal fin (clamped or pinned), and the natural curvature of the tail at rest. During the experimental tests, the flapping of prototypes was captured by a digital camera (IDS UI-3370SE-M-GL) under controlled illumination conditions.

4. Characterization of the propulsion capacity

We start by testing the prototypes shown in Fig. 2(c), which we refer to as "layout 1" (L1). They follow the design of Fig. 1(a), with a clamped fin at the tip, while varying the number of segments ($4 \leq n \leq 8$). The experimental results for the mean thrust force $\bar{F}_x$ (average value in the cycle), as a function of the actuation frequency f are reported in Fig. 3(a). Each dataset corresponds to a prototype with a set number n of segments; the data points refer to the average of five measurements, and the corresponding standard deviations are represented as error bars. A fitted spline serves as a guide to the eye of each dataset. For each prototype, we find an optimal frequency value that provides maximal thrust: the decreasing branch corresponds to oscillations progressively becoming less symmetric, until the beam can no longer snap because the actuation is too fast to overcome inertial and viscous forces. The tails with $n = 6$ and $n = 7$ segments provide approximately the same maximum for $\bar{F}_x$. For the longest prototype $n = 8$, the motion becomes soon unstable when the actuation frequency increases. For the short prototypes, $n = 4$ and $n = 5$, the expected peak value of $\bar{F}_x$ is not reached in the accessible range of frequencies, which could not be increased further without producing excessive vibrations in the experimental apparatus. Overall, the prototype with $n = 7$ provided the best compromise between thrust generation and smooth motion, therefore, becoming the reference for subsequent tests.

Having set $n = 7$, we proceeded by investigating whether a modification of the shape of the segment cavities, providing different curvatures for the tail at rest, could enhance thrust. Hence, we introduce the "layout 2" (L2) prototype, which is "less bent" at rest than "layout 1" (L1). For a quantitative characterization of the difference, at each segment i we define the curvature $\chi_i = 1/r_i$, where r_i is the radius of the circle passing through the centroids of segments i, $i+1$ and $i-1$. The difference between the L1 and L2 prototypes is shown in the left- and right-hand illustrations of Fig. 3(b), respectively juxtaposing the values of χ_i, for $i = 3 \ldots 6$ (Fig. 3(b).1), and the shapes at rest (Fig. 3(b).2). Fig. 3(c) compares the mean thrust $\bar{F}_x$: the response is similar between the L1 and L2 cases, except for a shift towards higher frequency for L2. Fig. 3(d) shows the time series of thrust F_x and transverse force F_y, at the actuation frequency corresponding to the peak thrust. Remarkably, the motion of the L2 tail was much smoother and symmetric (compare the plots of F_y) than the L1 tail. The high-frequency oscillations, which have been low-passed in the graphs of Fig. 3(d), correspond to the noise due to reflections from the walls and interactions of the waves generated by the moving tail within the tank, as well as to the snapping itself, which occurs like a whiplash. The more bent shape (at rest) of the L1 tail provides a more powerful snapping and a longer path of the fin, but this dissipates more energy in the lateral direction, producing more waves and causing more undesired vibrations. The milder and smoother snapping sequence of the L2 tail generates less noise in the measured force and is more efficient. Because of this finding, the L2 prototype with 7 segments was chosen as the new reference for the subsequent steps of our investigation.

In all of the experiments above, the prototypes were equipped with a clamped PMMA fin. Based on recent studies [26] suggesting that a pivoting fin may increase performance, we performed
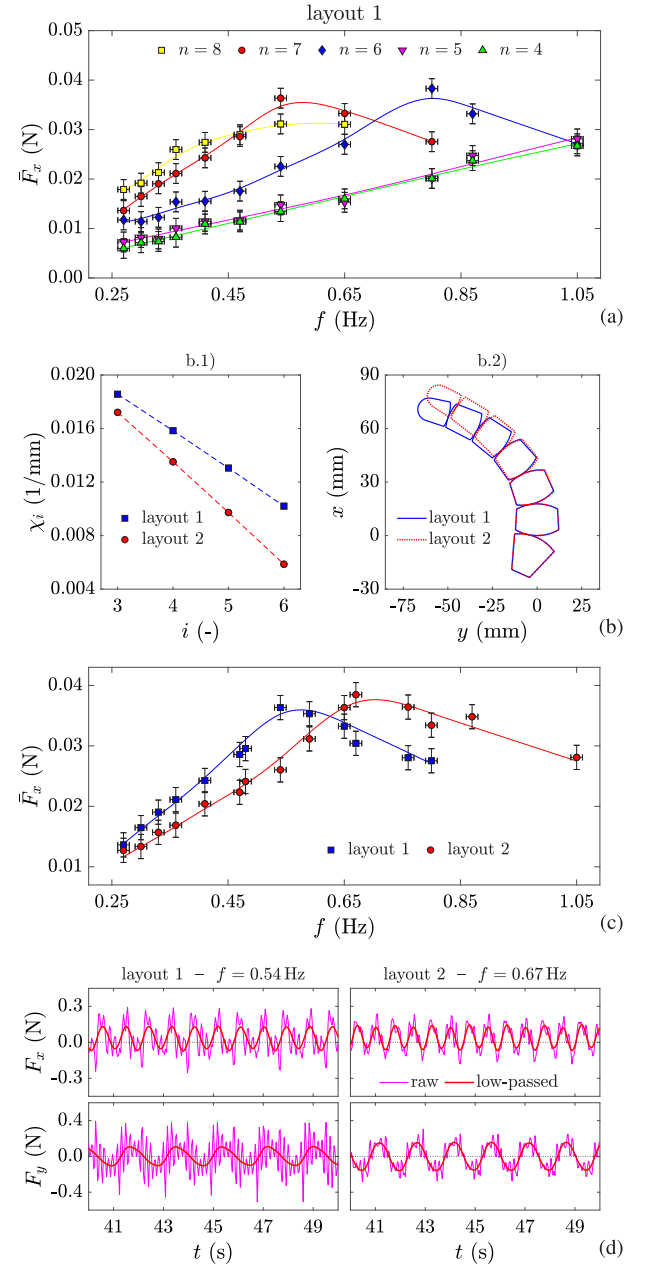
Fig. 3. Experimental results for the snapping tail with a fixed fin. (a) Mean thrust force $\bar{F}_x$ as a function of the actuation frequency f, for tails with a different number of segments ($4 \leq n \leq 8$) in the "layout 1". (b) Characterization of "layout 1" and "layout 2" for tails with $n = 7$ segments in terms of: (b.1) curvature χ_i at the i-th segment, $i = 3 \ldots 6$, and (b.2) reference shapes at rest. (c) Mean thrust force $\bar{F}_x$ as a function of frequency f for "layout 1" and "layout 2" with $n = 7$ segments. (d) Time series of the recorded thrust (F_x) and transverse force (F_y), at the frequency of peak mean thrust.

a new set of experiments in which the fin was pinned (instead of clamped) at the tip of the tail. This fin could rotate freely, within an angular range $\pm\vartheta$, as per Fig. 2(d).2. We considered five different cases with $\vartheta = 15°, 25°, 35°, 45°, 55°$. Fig. 4(a).1 shows the measured mean thrust $\bar{F}_x$ as a function of the frequency f, for the L2 prototype with 7 segments and pinned fin, for different values of ϑ (each point corresponds to the average of five measurements). Fig. 4(a).2 reports the corresponding peak thrust as a function of ϑ, evidencing that a maximum is obtained around 30°. These results confirm that the pinned fin allows
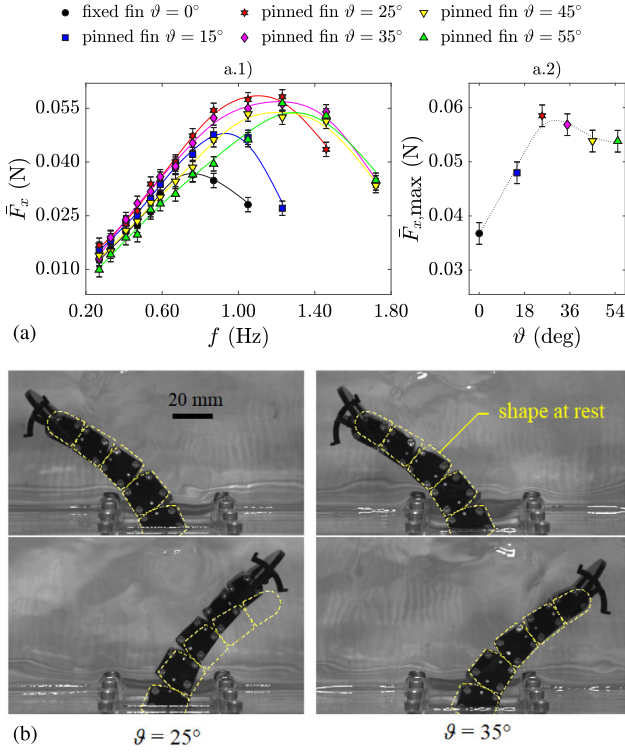
Fig. 4. Experimental results for the "layout 2" prototype with $n = 7$ segments and pinned fin. (a) Measurements of generated thrust: (a.1) mean thrust force $\bar{F}_x$ as a function of the actuation frequency f, for various limit angle ϑ for the fin, and (a.2) corresponding peak value of the mean thrust force as a function of ϑ. (b) Comparison between the extremal configurations during the motion at $f = 1.05$ Hz, corresponding to the peak thrust, for $\vartheta = 25°, 35°$ (shapes at rest are drawn, for reference, in yellow color). The video from which the snapshots are taken is available as supplementary material. (For interpretation of the references to color in this figure legend, the reader is referred to the web version of this article.)

attaining a more favorable angle of attack in the fluid, enhancing the thrust generated.

The case with $\vartheta = 25°$ provides the highest measured thrust at $f = 1.05$ Hz; however, the frames from the video, reported in Fig. 4(b), indicate that the motion lacks symmetry and is not fully developed, as evidenced by the comparison with the theoretical rest shape (dashed yellow lines). Under these conditions, the actuation is too fast compared to the inertial and viscous forces. Therefore, for the field application that we will present in Section 5 for a toy vessel propelled by one single snapping tail, we will choose the case $\vartheta = 35°$ at the same frequency $f = 1.05$ Hz. From Fig. 4(b), this case corresponds to symmetric oscillations at the cost of a (small) thrust loss of about 4%. In any case, the gain of thrust with respect to the clamped fin is more than 40%, passing from 38 mN for $\vartheta = 0°$ at $f = 0.67$ Hz to 55 mN for $\vartheta = 35°$ at $f = 1.05$ Hz. Note that symmetric oscillations should be considered a design requirement to avoid parasitic deflections of the vessel trajectory when one tail is used for propulsion; to achieve a nearly straight motion, the transverse force F_y at one stroke needs to be compensated by an equal force in the opposite direction at the following stroke.

5. Field application of the flexural-tensegrity snapping tail

As a proof-of-concept application in a field setting, we equipped a toy vessel with a snapping tail for propulsion and tested it in a rectangular fountain basin (see photograph in Fig. 5(a)). The top view of the moving vessel was video recorded
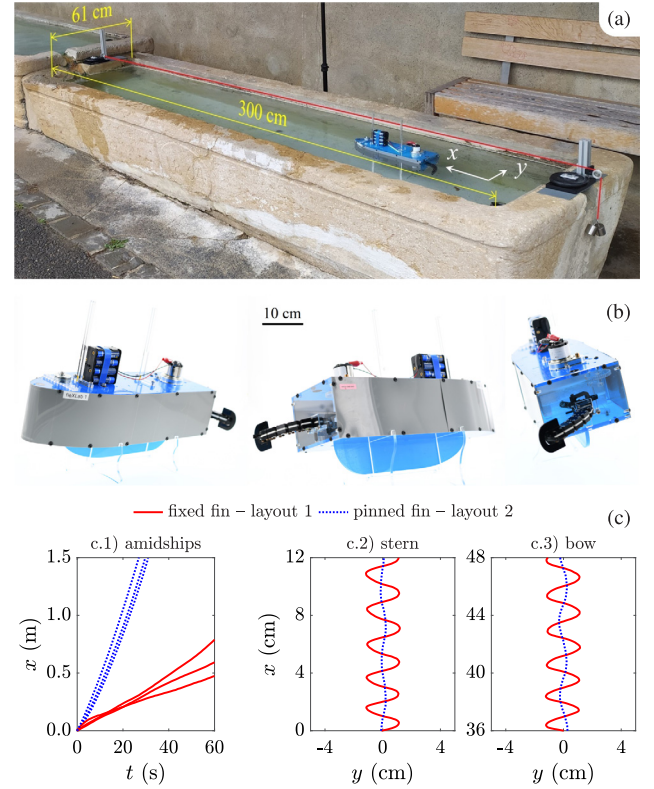
Fig. 5. Field application of a toy vessel propelled by a flexural-tensegrity snapping tail. (a) View of the basin for the test, indicating the main dimensions, reference frame, and the guidewire (highlighted in red color). (b) Photograph of the manufactured vessel, evidencing the propulsive tail, the motor, the battery holder, and the keel. A video of the sailing toy vessel, equipped with the most performing L2 tail with pinned fin, is available as supplementary material. (c) Experimental results comparing the performance of a vessel propelled either by the 7-segment "layout 1" tail and fixed fin, actuated at $f = 0.54$ Hz, or by the "layout 2" tail with movable fin (limit angle $\vartheta = 35°$) at $f = 1.05$ Hz: (c.1) vessel position x (amidships) as a function of time t, and trajectories of (c.2) the stern and (c.3) the bow. (For interpretation of the references to color in this figure legend, the reader is referred to the web version of this article.)

using a digital camera (Samsung S5KGM1). The $300 \times 61 \times 50$ cm³ tank had a water inlet on its left-hand side and an outlet on its right-hand side, with a morning-glory spillway producing a background flow with surface velocity estimated to be ≈ 9 mm/s. A wire (highlighted in red in Fig. 5(a)), kept straight by a hanging weight through a pulley, guided the vessel in the x-direction of the reference frame indicated in the same picture. This guidewire was needed because the vessel had no active control against external disturbances, such as wind.

Both vessel and tail, shown in Fig. 5(b), were manufactured out of laser-cut acrylic plates and polypropylene shim stock, and bolted together. The interior of the boat was filled with polystyrene foam to increase buoyancy, while a vertical keel was used to improve stability. The hull was 38 cm long, with a tail of length approximately 12 cm, including the fin. The tail was submerged in water to a depth of 5 cm (same depth of the in-lab tests); it was actuated, through crank and crankshaft, by the same motor used in the experimental setup of Section 3. Two types of tails with $n = 7$ segments were considered: the L1 prototype with *fixed fin*, actuated at $f = 0.54$ Hz, and the L2 prototype equipped with a *pinned fin* with limit angle $\vartheta = 35°$, at $f = 1.05$ Hz. The first case corresponds to the highest mean thrust force, as per Fig. 3(a); the second one to the best compromise between thrust and regularity of motion, according to Figs. 4(a) and 4(b).

Fig. 5(c) reports quantitative results for the motion of the vessel sailing in the fountain basin. The left-hand plot (Fig. 5(c).1) shows the x-position of the boat as a function of time t: the propulsion speed dx/dt is ≈ 0.011 m/s for the L1 tail with fixed fin, and ≈ 0.049 m/s for the L2 tail with pinned fin, confirming in the field the advantages of the second design, as already indicated by in-lab experiments. Since the reference frame of Fig. 5(a) is integral with the tank, dx/dt is the absolute speed; the relative speed with respect to the fluid is obtained by summing up the background flow. The trajectories of stern (Fig. 5(c).2) and bow (Fig. 5(c).3), represented in the two plots on the right-hand side of Fig. 5(c), evidence the yawing motion for a vessel propelled by the L1 tail, which determines undesired oscillations and waste of energy in lateral propulsion. The situation improves remarkably for the L2 tail with pinned fin, confirming that this is the best design among all those considered.

In order to compare our vessel with a swimming fish, reference can be made to the Strouhal number (St). This traditionally defines a similarity index for wakes and frequency of vortex formation behind flow obstructions, but can also be applied to the alike wake structures generated by flapping foils in a fluid. For a swimming fish, St can be defined [4] as $St = 2Af/V$, where A is the amplitude of oscillations for the tail beating at frequency f, and V represents the velocity of the fish with respect to the fluid. Fishes generally swim at $St \simeq 0.3$ [6], considered a bio-motivated optimal value. For the toy vessel, with a background flow of 0.009 m/s, one has $V = 0.020$ m/s for the L1 tail and $V = 0.058$ m/s for the L2 case. Assuming $A \simeq 60$ mm, as measured in the tests, one obtains $St = 3.24$ and $St = 2.17$ for the L1 and L2 prototypes, respectively. These values are still considerably higher than for a fish, indicating that there is ample room for improvement and further optimization in the design of both the hull and the propelling tail. Still, the Strouhal number closer to that of the fish corresponds to the L2 layout with pinned fin, confirming its superiority with respect to the L1 prototype with fixed fin.

6. Conclusions

We have investigated the possibility, as an experimental proof-of-concept, of using flexural-tensegrity beams as propulsion mechanisms to mimic fish swimming. Our device comprises a cantilever made of segments held in contact by a prestressing tendon, susceptible to an ordered snap in response to a localized perturbation (relative rotation of the two terminal segments). The shape of the contact surfaces dictates the constitutive properties, and the snap is due to the mobility of the tendon within properly-shaped cavities of the segments. The structure can be activated cyclically, acting as a flagellating tail. We have characterized the propulsion capacity by parametrically varying the number of segments and the shape of their internal cavities, also considering the effect of a terminal fin, either clamped or hinged to the cantilever tip. The concept has been demonstrated for the propulsion of a toy vessel.

Our results suggest that the flexural-tensegrity concept of the snapping cantilever should find application in marine propulsion, thanks to the following properties: (i) the motion is autonomous, once it is triggered by the rotation of one joint, and (ii) can be reversed by changing the sign of actuation; (iii) the driving system is a simple crank and crankshaft mechanism, connected to a motor at low revs; (iv) the system is robust, since the segments are massive and the tendon can be a braided strand, to avoid collapse if one wire breaks; (v) the tail can be used both as a propeller and a rudder, by actively controlling the driving motor.

We have also identified the following limitations, which we hope will be addressed by future studies. For the cantilever and the tip fin, just a few elementary schemes were considered, which are presumably far from being optimal; flexible flappers with profiled geometries could be added; a limited range of frequencies was tested only in water; theoretical modeling of the fluid–structure interaction is needed to rationalize the blending between elastic and inertial forces, together with drag and viscous forces in the fluid. Furthermore, to evaluate the real advantages of our system, it will have to be compared with other types of non-snapping simple flappers.

Nevertheless, whereas our study was framed as a proof-of-concept, our findings point to exciting new avenues for future investigations on bio-inspired flexural-tensegrity propulsion. Potential applications could be considered at different length scales: microthrusters for medical microrobots, capable not only of swimming in highly viscous human fluids, but also of climbing blood vessel walls or acting as stents; amphibious vehicles to move in marshes; submarines with silent biomimetic propulsion. Who knows? Perhaps Jules Verne could have imagined flexural tensegrities twenty thousand leagues under the seas.

Funding

CRediT authorship contribution statement

Claudio Boni: Design of flexural-tensegrity structures, Built the prototypes, Designed and carried out the experiments, Writing - Original Draft. **Pedro M. Reis:** Designed and carried out the experiments, Writing - Original Draft. **Gianni Royer-Carfagni:** Design of flexural-tensegrity structures, Writing - Original Draft.

Declaration of competing interest

The authors declare that they have no known competing financial interests or personal relationships that could have appeared to influence the work reported in this paper.

Data availability

Data will be made available on request.

Appendix A. Supplementary data

Supplementary material related to this article can be found online at https://doi.org/10.1016/j.eml.2022.101853. Supplementary material includes: (1) a video of a transparent tail snapping in the air, to evidence the driving mechanism of the structure; (2) the source video for the snapshots of Fig. 4(b); (3) a video of the sailing toy boat of Fig. 5.

References

[1] I. Nesteruk, G. Passoni, A. Redaelli, Shape of aquatic animals and their swimming efficiency, J. Mar. Biol. 2014 (2014).

[2] J. Ohlberger, G. Staaks, F. Hölker, Swimming efficiency and the influence of morphology on swimming costs in fishes, J. Comp. Physiol. B 176 (1) (2006) 17–25.

[3] R. O'Dor, Telemetered cephalopod energetics: Swimming, soaring, and blimping, Integr. Comp. Biol. 42 (5) (2002) 1065–1070.

[4] E.D. Tytell, I. Borazjani, F. Sotiropoulos, T.V. Baker, E.J. Anderson, G.V. Lauder, Disentangling the functional roles of morphology and motion in the swimming of fish, Integr. Comp. Biol. 50 (6) (2010) 1140–1154.

[5] M. Sfakiotakis, D.M. Lane, J.B.C. Davies, Review of fish swimming modes for aquatic locomotion, IEEE J. Ocean. Eng. 24 (2) (1999) 237–252.

[6] M.S. Triantafyllou, G.S. Triantafyllou, An efficient swimming machine, Sci. Am. 272 (3) (1995) 64–70.

[7] S. Coyle, C. Majidi, P. LeDuc, K.J. Hsia, Bio-inspired soft robotics: Material selection, actuation, and design, Extreme Mech. Lett. 22 (2018) 51–59.

[8] R.K. Katzschmann, A.D. Marchese, D. Rus, Hydraulic autonomous soft robotic fish for 3D swimming, in: Experimental Robotics, Springer, 2016, pp. 405–420.

[9] R.K. Katzschmann, J. DelPreto, R. MacCurdy, D. Rus, Exploration of underwater life with an acoustically controlled soft robotic fish, Science Robotics 3 (16) (2018).

[10] R. Taggart, Novel marine propulsion devices, J. Amer. Soc. Naval Eng. 70 (4) (1958) 643–652.

[11] C. Boni, G. Royer-Carfagni, Energy harnessing in the snap-through motion of a flexural-tensegrity flagellum, Mech. Mach. Theory 173 (2022) 104845.

[12] C. Boni, M. Silvestri, G. Royer-Carfagni, Flexural tensegrity of segmental beams, Proc. R. Soc. A 476 (2237) (2020) 20200062.

[13] C. Menn, Prestressed Concrete Bridges, Birkhäuser Verlag, Basel, 1990.

[14] C. Boni, G. Royer-Carfagni, Nonlinear effects in the vibrations of flexural tensegrity beams, Int. J. Non-Linear Mech. 128 (2020) 103616.

[15] C. Boni, G. Royer-Carfagni, Equilibrium of bi-stable flexural-tensegrity segmental beams, J. Mech. Phys. Solids 152 (2021) 104411.

[16] C. Boni, G. Royer-Carfagni, A nonlocal elastica inspired by flexural tensegrity, Internat. J. Engrg. Sci. 158 (2021) 103421.

[17] C. Boni, G. Royer-Carfagni, A new flexural-tensegrity bow, Mech. Mach. Theory 164 (2021) 104398.

[18] P. Handral, R. Rangarajan, An elastica robot: Tip-control in tendon-actuated elastic arms, Extreme Mech. Lett. 34 (2020) 100584.

[19] C.-Y. Yeh, S.-C. Chou, H.-W. Huang, H.-C. Yu, J.-Y. Juang, Tube-crawling soft robots driven by multistable buckling mechanics, Extreme Mech. Lett. 26 (2019) 61–68.

[20] C.-Y. Yeh, C.-Y. Chen, J.-Y. Juang, Soft hopping and crawling robot for in-pipe traveling, Extreme Mech. Lett. 39 (2020) 100854.

[21] Z. Vangelatos, G.X. Gu, C.P. Grigoropoulos, Architected metamaterials with tailored 3D buckling mechanisms at the microscale, Extreme Mech. Lett. 33 (2019) 100580.

[22] A.J. Smits, Undulatory and oscillatory swimming, J. Fluid Mech. 874 (2019).

[23] T. Van Buren, D. Floryan, D. Brunner, U. Senturk, A.J. Smits, Impact of trailing edge shape on the wake and propulsive performance of pitching panels, Phys. Rev. Fluids 2 (1) (2017) 014702.

[24] P. Leroy-Calatayud, M. Pezzulla, A. Keiser, K. Mulleners, P.M. Reis, Tapered foils favor traveling-wave kinematics to enhance the performance of flapping propulsion, Phys. Rev. Fluids 7 (2022) 074403.

[25] P.D. Yeh, Y. Li, A. Alexeev, Efficient swimming using flexible fins with tapered thickness, Phys. Rev. Fluids 2 (10) (2017) 102101.

[26] Q. Zhong, J. Zhu, F.E. Fish, S.J. Kerr, A.M. Downs, H. Bart-Smith, D.B. Quinn, Tunable stiffness enables fast and efficient swimming in fish-like robots, Science Robotics 6 (57) (2021) eabe4088.